



Versatile Neuromorphic Modulation and Biosensing based on N-type Small-molecule Organic Mixed Ionic-Electronic Conductors

Riping Liu⁺, Xiuyuan Zhu⁺, Jiayao Duan, Junxin Chen, Zhuang Xie, Chaoyue Chen, Xi Xie, Yanxi Zhang, and Wan Yue*

Abstract: The ion/chemical-based modulation feature of organic mixed ionic-electronic conductors (OMIECs) are critical to advancing next generation bio-integrated neuromorphic hardware. Despite achievements with polymeric OMIECs in organic electrochemical neuronal synapse (OENS). However, small molecule OMIECs based OENS has not yet been realized. Here, for the first time, we demonstrate an effective materials design concept of combining n-type fused all-acceptor small molecule OMIECs with subtle side chain optimization that enables robustly and flexibly modulating versatile synaptic behavior and sensing neurotransmitter in solid or aqueous electrolyte, operating in accumulation modes. By judicious tuning the ending side chains, the linear oligoether and butyl chain derivative gNR-Bu exhibits higher recognition accuracy for a model artificial neural network (ANN) simulation, higher steady conductance states and more outstanding ambient stability, which is superior to the state-of-art n-type OMIECs based OENS. These superior artificial synapse characteristics of gNR-Bu can be attributed to its higher crystallinity with stronger ion bonding capacities. More impressively, we unprecedentedly realized n-type small-molecule OMIECs based OENS as a neuromorphic biosensor enabling to respond synaptic communication signals of dopamine even at sub- μM level in aqueous electrolyte. This work may open a new path of small-molecule ion-electron conductors for next-generation ANN and bioelectronics.

Introduction

Organic neuromorphic electronics inspired by human brain to imitate the learning and memory functions of the central nervous system, hold unprecedentedly promising applications in brain-machine interaction, neuroscience, and artificial intelligence, due to versatile advantages over traditional silicon-based electronics in massive parallelism,^[1] low operating voltage and energy consumption,^[2] mechanical compliance,^[3] biocompatibility,^[4] and responsivity to chemical signals.^[5] Artificial synapse as the functional connection between neurons to transmit neurotransmitter signals is the cornerstone to construct brain-like artificial networks (Figure 1a), where the ability to incorporate ion modulation is essential to mimic various synaptic behavior.

Organic electrochemical transistors (OECTs), a typical class of electrolyte-gated transistors,^[6] have been demonstrated as a promising platform for developing organic electrochemical neuronal synapse (OENS) due to its similar underlying principle with biological nervous system.^[7] Similar to the ion/neurotransmitter-induced electric signal generation and transmission in nervous systems,^[8] the operation of OECTs are also dominated by ion migration through the electrolyte and ion-electron interfacial coupling in the channel materials. Thus OECTs with the three-terminal configurations could be an analogue to the biological synapses.^[9] The channel conductance modulated by ion migration corresponds to the synaptic weight (SW), which is closely related with activity-dependent changes in neuron networks and is fundamental to neuromorphic computing.

Despite various neuromorphic functions based on OENS achieved before, such as short-term plasticity (STP), long-term plasticity (LTP), and spiking-timing-dependent plasticity (STDP) and spiking-voltage-dependent plasticity

[*] R. Liu,⁺ X. Zhu,⁺ J. Duan, J. Chen, Prof. Z. Xie, C. Chen, Prof. W. Yue
 Guangzhou Key Laboratory of Flexible Electronic Materials and Wearable Devices, Key Laboratory for Polymeric Composite and Functional Materials of Ministry of Education, School of Materials Science and Engineering, State Key Laboratory of Optoelectronic Materials and Technologies, Sun Yat-sen University
 510275 Guangzhou (P. R. China)
 E-mail: yuew5@mail.sysu.edu.cn

Prof. X. Xie
 Institute of Precision Medicine, The First Affiliated Hospital Sun Yat-sen University, State Key Laboratory of Optoelectronic Materials and Technologies, Guangdong Province Key Laboratory of Display Material and Technology, School of Electronics and Information Technology, Sun Yat-sen University
 510006 Guangzhou (P. R. China)
 Prof. Y. Zhang
 The Institute of Flexible Electronics (IFE, Future Technologies), Xiamen University
 361005 Xiamen, Fujian (China)

[⁺] These authors contributed equally to this work.

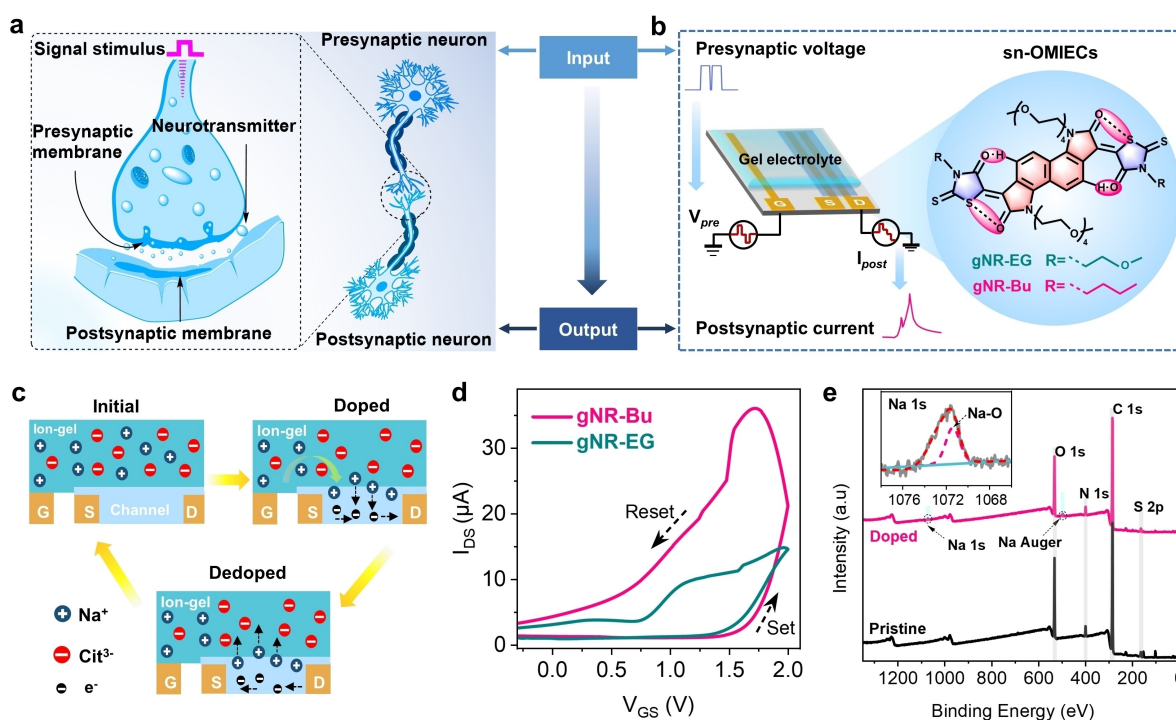


Figure 1. Schematic illustration of a) a biological synapse and b) an organic electrochemical neuronal synapse based on small-molecular n-type OMIECs. Just as biological synapses connect two neurons to communicate modulated by signal stimulus, small-molecular n-type OMIECs serve as the synaptic weight to mimic synaptic behaviors gated by mixed ion-to-electron transduction. c) Schematic of the electrochemical doping and dedoping processes. d) Transfer curve of gNR-EG and gNR-Bu device. e) XPS of representative gNR-Bu film in pristine and doped states and inset is the emerged Na 1s XPS spectrum of doped gNR-Bu film.

(SVDP) behaviors,^[1,10] et al., thus far multifunctional neuromorphic modulating in a single device remains challenging, especially with high stability and outstanding performances. Additionally, the simulations of synaptic behavior are mostly based on solid-state devices,^[11] which differs the real operation conditions of biological synapses. The shielding effect in an aqueous media results in inability to regulate ions movement to generate memory.^[12] It is so still a great challenge to simulate the real biological synapse, especially to achieve the neuromorphic functions in aqueous or biological environments.

As the critical component of OENS, the channel layer is tailorable organic mixed ionic-electronic conductors (OMIECs). The robust synaptic plasticity depends on high-performance OMIECs to efficiently support the fast transport of ionic and electronic species, to retain a broad range of conductance states after the voltage spiking, and to allow high environmental stability. However, OMIECs for OENS are commonly p-type polymers, the n-type OMIECs are rare in artificial synapses.^[13] However, n-type OMIECs are indispensable for complementary circuits and biosensors for metabolites and monitor cation movements where electron transfer processes occurred.^[14] For example, depletion mode OECT based p-type poly(3,4-ethylenedioxythiophene)-poly(styrenesulfonate) (PODOT:PSS) was reported to be artificial synapse for non-electroactive biomolecules as well as for low highly sensitive sensing of dopamine.^[15] While for the low consumption accumulation-mode OESN based

dopamine biosensor where a positive gate voltage was applied for the devices to cause the redox reaction of dopamine, an n-type OMIECs channel is necessary, while have not been reported so far. Such neurotransmitters sensing based on n-type OMIECs with typical of large amplification is significantly superior to the amperometric sensors in term of sensitivity, detection limits and stability, which conduces to accurately and sensitively detect analyte for medical diagnosis.^[16] It is thus urgent to develop suitable n-type OMIECs for such enhancement-mode neurotransmitter assay. The fundamental challenge of n-type OMIECs implementation is the instability of electronic charges in air under ambient conditions.^[13a] Deep lowest unoccupied molecular orbital (LUMO) levels below -4 eV are necessitated to avoid side reactions and realize a sufficient number of electrons.^[2] Thereby, the design and synthesis of n-type OMIECs for OENS with low LUMO levels to achieve versatile neuromorphic modulating with excellent ambient stability remains extremely challenging.

Compared with polymeric OMIECs, small-molecule OMIECs also have the low-cost and high-throughput solution processable capability, whereas display obvious merits including flexible tailoring for electronic structures, the ease of tunable synthesis and ease purification, well-defined chemical structure with monodisperse nature.^[17] The accurate structure-property relationships along with the absence of chain entanglements facilitate microstructure control and enhancement of device performance in organic

electronic application such as organic field-effect transistor,^[18] solar cells.^[19] This class of mixed conductors recently attracted great attention for the emerging field of OECTs.^[17a] Thereby, they are viable candidates for developing high-performance organic neuromorphic electronics. So far, however, small-molecule n-type OMIECs (sn-OMIECs) have not been reported for the development of OENS owing to the materials scarce and lacking the efficient molecular design strategies.

Herein, we reported, for the first time, two small-molecule n-type OMIECs based organic electrochemical neuronal synapse (sn-OENS), which not only successfully mimics versatile neuromorphic functions gated by solid-state gel electrolytes but also achieves the sensing of dopamine (DA) neurotransmitter in an aqueous environment. In the solid-state devices, versatile synaptic properties are accomplished in a single sn-OENS, including robust tunability of synaptic plasticity (e.g., STP, LTP, STDP and SVDP), learning and memory, signal separation, dynamic filtering, and image recognition. Remarkably, OENS with gNR-Bu displays a high recognition accuracy of 94 % for a model artificial neural network, highly steady conductance states maintained over 600 s in ambient conditions, as well as excellent ambient stability with the current retained by 54 % after 100 days without any encapsulating, or further improving to 90.9 % via briefly adjusting gate voltage as compensation, which is remarkably superior to previous n-type organic synapses. More impressively, in aqueous electrolyte gated pattern, our gNR-EG and gNR-Bu based devices enable to sense synaptic communication signals like DA even at sub- μM level.

Results and Discussion

Noncovalent conformation locks strategy has become an important method to design and synthesize highly planar and rigid conjugated system for high performing organic semiconductors in organic electronics.^[20] Here, our novel sn-OMIECs were designed via an intramolecular conformation lock strategy by combining S–O interaction and hydrogen bond.^[17b] The strong noncovalent S–O interaction between the sulfur atom at the ending rhodamine motifs and the oxygen atom into the lactam rings as well as the hydrogen bond between the oxygen of the rhodamine and the hydrogen of the naphthalene contribute to their fused and planar π -conjugated structures, enabling efficient electronic conduction. The ethylene glycol (EG) side chains allow good solubility for further solution-processing and adequate ionic pathways. We utilized the imide positions of rhodamine to link two different types of side chains: the hydrophilic EG chain (gNR-EG) and the hydrophobic linear butyl chain (gNR-Bu). For a better comparison of their properties and synapse functions, the EG side chain of gNR-EG and the linear butyl chain have the same length. The detailed information about the synthesis and characterization for gNR-EG and gNR-Bu are described in Supporting Information.

Both n-type small-molecule OMIECs can serve as synaptic weight-active channel of OENS gated by solid gel (or aqueous) electrolyte to accomplish controlled doping and de-doping (Figure 1b). Just as the working process of biological synapse: triggering action potential, releasing neurotransmitter and receiving electrical signals, Figure 1c illustrates a schematic of the electrochemical doping and de-doping processes of our sn-OENS. By applying a positive presynaptic voltage ($V_{\text{pre}} = 2.0 \text{ V}$), i.e., the V_{G} , to generate action potentials, the cations from electrolytes (Na^+), which resemble the “neurotransmitters”, can inject into the active channel, thus triggering an excitatory postsynaptic current (EPSC) resulting from electrons generated in the channel between the source and drain electrodes. For the de-doping process under a negative voltage (-0.3 V), ions are expelled from the channel into the electrolyte driven by electric field. Notably, the de-doped state was found to not fully recover to its initial neutral state due to the partly maintained Na^+ in the channel even under negative voltages, providing the basis of non-volatile properties and synapse plasticity.^[21] Next, we fabricated the OENS employing a simple planar transistor architecture with the gate close to the channel by thermal evaporation technology, which is gated by a gelatin-based solid-state electrolyte containing sodium citrate (Figure 1b). Notably, complex and expansive photolithography technology have not been utilized for our OENS devices preparation, which is necessary for most of vertical or stacked OENS device structures.^[1,14] Such solid-state electrolyte prepared by simply immersing a gelatin-glycerol/sodium citrate mixture solution (See the Supporting Information), has been proved to a viable multifunctional candidate for electrolyte, electrodes and substrates,^[22] due to its high toughness, healing capabilities, long-term stability and adhesion.^[23] And the solid-state gel electrolyte was utilized to improve the ion retaining in the channel by reducing the spontaneous ion migration under “off” state, as well as the environmental stability.^[24] From the transfer curves of the as-fabricated OENS (Figure 1d and S1), it clearly demonstrated the conductance switching process from the initial “off” state to the “on” state upon sweeping the V_{G} to 2 V, as well as the incompletely recovered initial state when the V_{G} finally returned to the negative. Note that gNR-Bu showed a larger hysteresis window and higher $I_{\text{on}}/I_{\text{off}}$ current ratio than those of gNR-EG, indicating robust tunability to synaptic plasticity. Moreover, we observed the changes of gNR-Bu film before and after Na^+ doping by the X-ray photoelectron spectra (XPS). In the doped film, the emergence of a new binding energy peak at 1072.18 eV is attributed to Na 1s and Na–O bond (Figure 1e and inset), along with 0.1 eV shift of O 1s peak in C–O–C bonds compared with pristine film (Figure S2), which directly proves that the cations injected into the gNR-Bu film and coordinate with oxygen atom of side chains after applying positive V_{G} bias.

Depending on the modulation of conductance, or the SW, the versatile synaptic behaviors of the OENS based on gNR-EG and gNR-Bu were systematically investigated. Firstly, short-term plasticity (STP), which plays a key role in filter out unnecessary information in human brain,^[25] was

mimicked by single-pulse-induced SVDP with varying pre-synaptic voltages (V_{pre}) ranging from 1.5 to 4.0 V. As shown in Figure 2a, the gNR-EG exhibited typical STP behavior that the induced EPSC fast returned to resting state once the V_{pre} was finished. In contrast, gNR-Bu shows obvious transition from volatility at $V_{\text{pre}}=1.5$ V to nonvolatility at $V_{\text{pre}}>2.0$ V, in which the EPSC could retain to a certain level for a while after the V_{pre} spike. For instance, the

retained EPSC after $V_{\text{pre}}=4.0$ V could achieve $\approx 6.8 \mu\text{A}$ for gNR-Bu, which was >3.5 -fold higher than that of gNR-EG. The EPSC peaks as a function of the V_{pre} are summarized in Figure S3, which indicates larger ranges of tunable EPSC for gNR-Bu devices than that of gNR-EG devices. Such a striking contrast between gNR-EG and gNR-Bu also exists in the single-pulse-induced STDP with different pulse durations (t_{pre}) ranging from 0.1 to 3.0 s (Figure 2b and S4). With the t_{pre} higher than 0.4 s at $V_{\text{pre}}=2.0$ V, the EPSC was discovered to not return to its initial value, leading to a series of conductance depending on the t_{pre} . Therefore, gNR-Bu exhibited the flexible tunability of STP from volatility to nonvolatility, which presents the potential for further versatile neuromorphic modulation. In addition, the sn-OENS also allowed ultralow power consumption. By reducing the readout voltage (1 mV), the energy consumption of single-pulse-induced spike can be declined to 2.19 pJ/spike for gNR-Bu device, lower than that of gNR-EG device for 24.03 pJ/spike (Figure S5). The low energy consumption feature with gNR-Bu is superior to previous n-type organic synaptic devices.^[26] Furthermore, we applied two successive pulses (2 V, $t_{\text{pre}}=0.5$ s) with various pulse intervals (Δt_{pre}) ranging from 0.1 s to 3.0 s to study the paired-pulse facilitation (PPF). The ratio of the second spike EPSC (A_2) to the first one (A_1) (Figure 2c inset), typically defined as the PPF index, can be used to evaluate the synaptic gain and the tunability. Upon the first pulse V_{pre} being removed (i.e., during Δt_{pre}), the counter ions diffused from the electrolyte into the channel and simultaneously interact with the induced electrons to reduce the EPSC, which is a dynamic equilibrium related to the Δt_{pre} . As shown in Figure 2c and S6, the gNR-Bu reached a maximum facilitation value of 205 % at $\Delta t_{\text{pre}}=0.1$ s and then gradually dropped to 126 % along with the increasing Δt_{pre} , exhibiting an advantage of robust tunability to paired pulses over previous works.^[26–27] In contrast, the tunable range of PPF index for gNR-EG was merely from 1.49 to 1.10. The curve of PPF index as a function of Δt_{pre} was fitted by a double exponential decay function with a formula: $\text{PPF index} = C_1 \cdot \exp(-\Delta t/\tau_1) + C_2 \cdot \exp(-\Delta t/\tau_2) + C_0$, where C_0 presents the PPF ratio gradually converges to 100 %, C_1 and C_2 are the weight of the paired-pulse facilitation process, and τ_1 and τ_2 are the characteristic relaxation times of the ion in the bulk and channel layer.^[25,28] The τ_1 and τ_2 of gNR-Bu were calculated for 0.10 s and 1.39 s, which is comparable to those in biological synapses.^[12]

Long-term plasticity (LTP), the foundation of neural learning and memory, can be achieved through STP transformed with perpetual training (e.g., pulse numbers) or stimulus intensity (e.g., pulse voltages). By applying ten continuous pulses ($V_{\text{pre}}=2.0$ V, $t_{\text{pre}}=1$ s, $\Delta t_{\text{pre}}=0.2$ s) to the gate, both gNR-EG and gNR-Bu devices displayed typical LTP behavior with the nonvolatile retention of EPSC over 50 s after removing the V_{pre} , which is extremely challenging for n-type organic synapses (Figure 2d). Impressively, gNR-Bu showed a higher memory level,^[29] in which the EPSC variations between its initial value and the steady-state EPSC could reach up to 2.2 μA , 4.4 times higher than those of gNR-EG (0.5 μA). Through applying ten consecutive

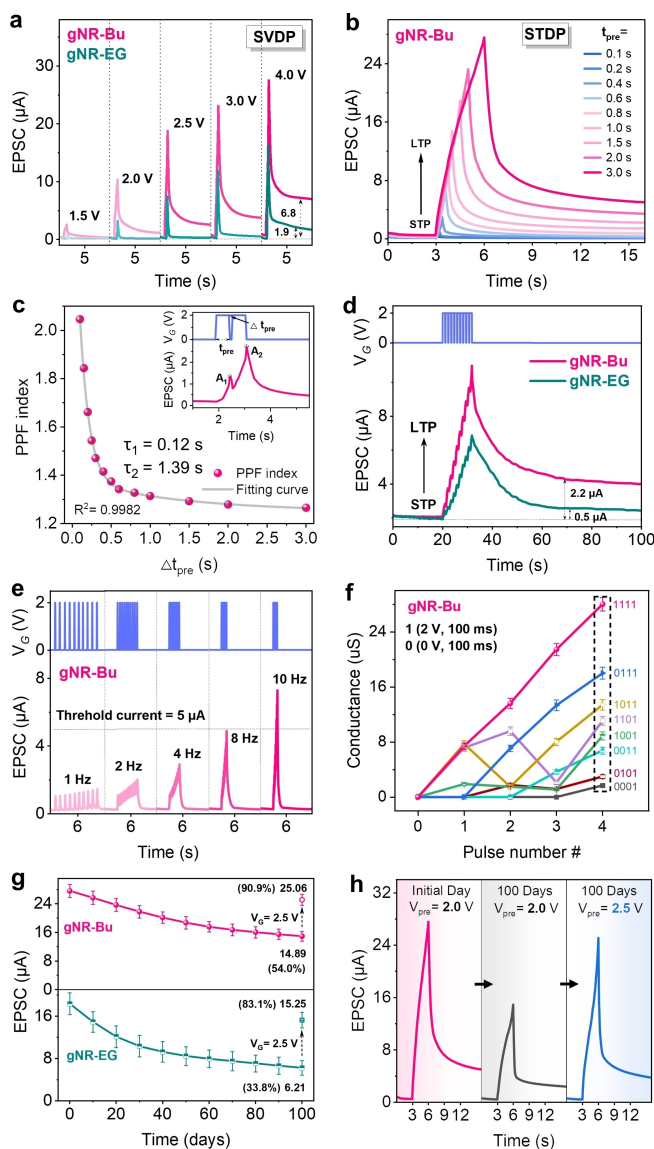


Figure 2. Versatile synaptic modes. a) SVDP of gNR-EG and gNR-Bu devices with different V_{pre} ranging from 1.5 to 4.0 V, under $V_{\text{SD}}=-0.5$ V, $t_{\text{pre}}=0.5$ s. b) STDP of gNR-Bu device with different t_{pre} ranging from 0.1 to 3.0 s, under $V_{\text{pre}}=2.0$ V, $V_{\text{SD}}=-0.5$ V. c) PPF index of gNR-Bu device. The red circle and gray line are the experimental PPF index and fitted result, respectively. The inset is a representative PPF of gNR-Bu device with $\Delta t_{\text{pre}}=0.1$ s. d) LTP behavior of gNR-EG and gNR-Bu devices. e) Dynamic filtering characteristics and f) separability of gNR-Bu device. g) EPSC results of the gNR-EG and gNR-Bu devices gated by single pulse in the ambient environment over 100 days. h) Comparison of EPSC spike of gNR-Bu device from the beginning to the 100th day ($V_{\text{pre}}=2.0$ V or $V_{\text{pre}}=2.5$ V).

pulses ($V_{\text{pre}}=2.0$ V, $t_{\text{pre}}=0.04$ s) with varied Δt_{pre} , we further studied the regulation of different pulse frequencies to achieve the dynamic filtering characteristic for processing input information. As shown in Figure 2e and S7a, the EPSC value of gNR-EG and gNR-Bu devices increased with the enhancement of the pulse frequency ranging from 1 to 10 Hz. However, the EPSC value of gNR-EG device maintained consistently below 5 μA that was defined as the threshold current value, while the EPSC value of gNR-Bu could distinctly exceed the threshold current once the frequency soared to 10 Hz. Thus, the high-frequency signals were considered to output when the EPSC value exceeds the threshold current, and on the contrary, those low-frequency signals were passed. To deeply investigate the filtering properties, the EPSC gain, defined as A_{10}/A_1 (Figure S7b), is used to evaluate the weight effect. The gNR-Bu showed greater amplification of EPSC gain ranging from 1.41 to 6.23 compared to those of gNR-EG (from 1.30 to 4.86). Therefore, the gNR-Bu demonstrated the high-pass filtering characteristic and gNR-EG could be used as a low-pass filter.

In addition to adjusting the pulse interval and duration, we manipulated the different triggering time-series of 4 continuous pulse spikes. To clarify, we defined different numbers and sequences for the four pulses, 0 and 1 indicating the pulse-state of 0 V (off) and 2 V (on), respectively. For example, an impulse sequence “1001” means that a 2 V pulse is applied first, followed by paired 0 V pulses, and finally a 2 V pulse, with same pulse duration (100 ms) for each one. As shown in Figure 2f and S8, eight pulse trains with different pulse sequences are applied (i.e., 0001, 0011, 0101, 1001, 0111, 1011, 1101, 1111), and the final output signals with different conductance state are indicated by the dashed box. This result implied that more pulse number (i.e., “1”) and later triggering timing can conduce to gain higher output signals, and thus different pulse sequences resulted in the output conductance states with different levels, which enables the separation of output signals.^[30] Interestingly, compared to gNR-EG, gNR-Bu exhibited better separability for different output signals modulated by different time-series pulses.

Besides, the ambient stability of n-type OMIECs based synaptic devices is critical to the real-world applications. N-type OMIECs relies primarily on electron transporting to conduct electricity, which makes it sensitive to moisture and oxygen in the air and thus results in its ambient instability. We employed the single pulse stimulation ($V_{\text{pre}}=2$ V, $V_{\text{SD}}=-0.5$ V, $t_{\text{pre}}=3$ s) to examine stability of the gNR-EG or gNR-Bu devices for up to 100 days (Figure 2g). Impressively, both devices displayed exceptional performance stability to obtain the EPSC by a voltage spike during the period of 100 days in ambient condition, with the peak values being retained for 54 % and 33.8 % for gNR-Bu and gNR-EG, respectively, which were further improved to 90.9 % and 83.1 % by slightly adjusting the V_{pre} to 2.5 V as compensation (Figure h and S9). Such self-repair behavior is of great significance in multifunctional neuromorphic computation and never revealed in previous artificial synaptic devices (Table S4). It is worth noting that the preceding

device fabrications and all tests are carried out in the ambient conditions without any encapsulating or further additional treating, demonstrating the potential of our sn-OENS in practical applications.

Based on the excellent non-volatility, we systemically studied the learning-experience behavior of gNR-Bu device to biologically simulate human brains and the capacity for mastering new information. Here, 40 continuous pulses with positive voltage of 2 V ($t_{\text{pre}}=0.13$ s, $\Delta t_{\text{pre}}=0.02$ s) were applied to mimic a learning process, followed by 40 continuous pulses with negative voltage (-1.5 V) to resemble the forgetting. As shown in Figure 3a, the first “learning” took about 6 s to reach the EPSC of 40 μA , and then EPSC gradually declined, representing the forgetting process. Noteworthy, after “learning”, the EPSC did not decrease to the initial value during the forgetting process with same time, indicating that accumulation is obtained by learning. Surprisingly, only 4 s was required for the second “learning” to reach the first level (EPSC=40 μA), and in the third “learning”, the time to reach previous level was further reduced to 2 s. Such feature is highly similar to humans learning-experience behavior principle, including multiple processes from receiving new information, forming short-term memory (STM) after initial learning and long-term memory (LTM) by long-term training, and to finally consolidating information (Figure 3b).

Beyond LTP and STDP, we also studied the long-term depression and potentiation (LTDP), which are significant metrics for analog neuromorphic computing. Cyclic LTDP behavior with 4000 cycles was accomplished by applying 40 repeated potentiation pulses ($V_{\text{pre}}=2.0$ V, $t_{\text{pre}}=0.26$ s, $\Delta t_{\text{pre}}=0.04$ s) and 40 repeated depression pulses ($V_{\text{pre}}=-1.0$ V, $t_{\text{pre}}=0.26$ s, $\Delta t_{\text{pre}}=0.04$ s) in each cycle. As shown in Figure 3c, the gNR-Bu device displays highly operating stability, wide analogue ranges up to 15 \times , linearity and symmetry over 4000 repeated LTDP cycles, which markedly surpasses previous n-type organic synapses (Table S4). The distinct conductance update was observed in each potentiation/depression process from the two reproducible LTDP shown in Figure 3d and inset. Contrastively, for gNR-EG, the rapid EPSC recovery after the voltage spike of 2.0 V led to poor LTDP properties (Figure S10). In addition, the performance of state retention serves as a foundation for large-scale homogeneous integration in ANN, therefore, the gNR-Bu device with 6 representative conductance states was evaluated in an open circuit with disconnected gate and source electrodes. As shown in Figure 3e, gNR-Bu device demonstrates the outstanding state retention across two orders of magnitude for over 600 s in ambient air, which sets the record of n-type organic synaptic devices.^[24,31] Overall, the conductance state retention, analog dynamic range, and the excellent ambient stability with synaptic functions of gNR-Bu is superior to the reported n-type polymeric OMIECs.

Based on the LTDP, we further implemented an analog three-layer network for training the backpropagation by a general method.^[10a,c,27,32] Figure 3f illustrates the schematic of the ANN including input layer, hidden layer and output layer. Artificial neurons (ANs) are indicated by circles, while the synaptic weights between the input ANs and

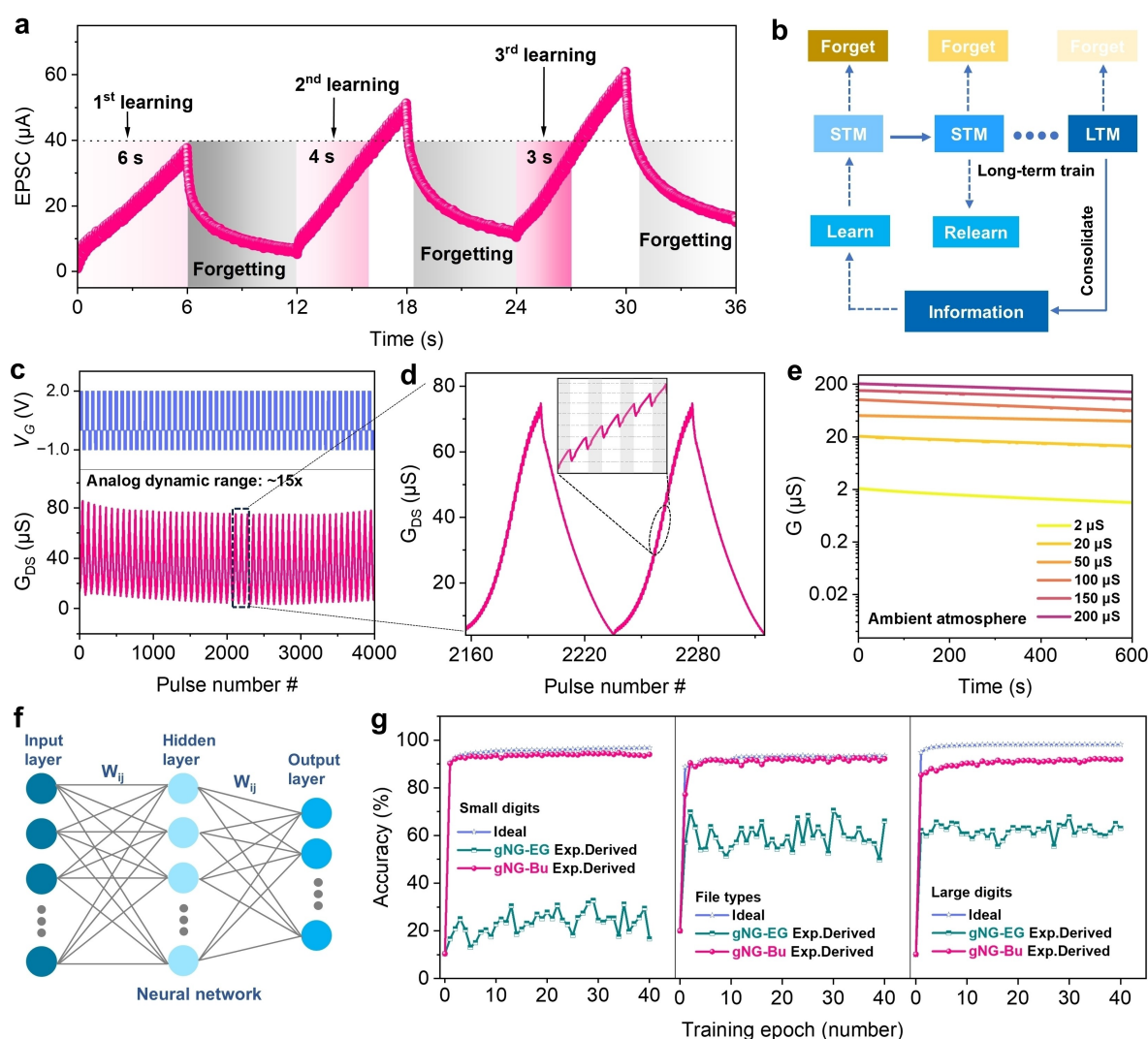


Figure 3. a) Learning-experience behavior of gNR-Bu device. b) The humans learning-experience behavior principle. c) Cyclic LTDP behavior of gNR-Bu device with 4000 pulses without an open gate circuit or current limiting resistor. 40 repeated potentiation pulses ($V_{pre} = 2.0$ V, $t_{pre} = 0.26$ s, $\Delta t_{pre} = 0.04$ s) and 40 repeated depression pulses ($V_{pre} = -1.0$ V, $t_{pre} = 0.26$ s, $\Delta t_{pre} = 0.04$ s) indicate a cycle. d) Two representative LTDP of gNR-Bu device with linear and symmetrical programming and magnified detail in inset. e) State retention of six representative analogue states of gNR-Bu device with an open gate circuit in the ambient environment. f) Schematic of a three-layer artificial neural network. g) Backpropagation training results of 8×8 pixel images (small), 28×28 pixel images (large) and Sandia file classification dataset based on the LTDP experimental data.

output ANs are represented by arrows. Artificial synapses connect all the neurons to each other. Here, we compared the analog performance of ANN with the three different datasets (an 8×8 pixel images (small) of handwritten digits from MNIST; a 28×28 pixel images (large) of handwritten digits; and a Sandia file classification dataset). As depicted in Figure 3g, after 40 cycles training for the ANNs, the gNR-Bu device shows a high accuracy near ideal numeric, reaching 94.0 % (small digits), 92.2 % (large digits) and 91.9 % (file types), respectively, which is significantly higher than those of gNR-EG device. Such high recognition accuracy for gNR-Bu benefiting from its good linearity, symmetry, and distinct conductance update, is comparable with the state-of-the-art organic synaptic devices, which makes it a promising candidate for analogue neuromorphic computing systems.

In order to explore the underlying principles for the difference between the synaptic behavior of the two sn-OMIECs, we performed detailed investigations on their optical and electrochemical properties. The two sn-OMIECs in solution and as thin films were first evaluated by Ultra-violet-visible near infrared absorption spectra and cyclic voltammetry (CV). Those relevant results are depicted in Figure S11–15 and summarized in Table S1. In both solutions and film states, both materials showed two prominent absorption characteristics with one absorption band in the 400–600 nm resulting from the $\pi-\pi^*$ transition and the other in the 600–1000 nm due to the intramolecular charge transfer (ICT) (Figure S11). Notably, when compared with the changes of absorption spectra in solutions and films, the gNR-Bu with butyl side chain exhibits a larger redshift of absorption maxima (62 nm) than those of gNR-EG with EG

chain (49 nm), indicating that the side chain without oxygen could facilitate aggregation in films and thus the formation of dense and ordered stacking structures, as well as enhanced interchain interactions.^[17b] In addition, gNR-Bu shows a larger absorption profile with a narrower optical band gap of 1.29 eV than that of gNR-EG of 1.37 eV, estimated by films absorption onsets (Table S1 and Figure S12–13), which could also be ascribed to the distinct molecular packing modes induced by the different side chains. Furthermore, deep LUMO levels of around -4.0 eV are calculated for gNR-Bu and gNR-EG, favoring electron injecting and transporting, concomitantly highly efficient n-type mixed ionic-electronic conduction, as well as diminishing electron trapping produced by water and oxygen, which provides the fundamentals for stable operation of n-type OMIECs in ambient air.^[13b,33] To reveal the electrochemistry doping mechanism, UV–vis–NIR spectroelectrochemistry was also used to study the electrochemical activity of thin films in synaptic modulation process. With stepwise reduction bias from 0.1 to -0.6 V (Figure S14), both gNR-EG and gNR-Bu films in aqueous solution exhibit a marked decline of the π – π^* and ICT absorption bands with simultaneous emergence of an increasing absorption band in the NIR region generated by the polaronic species.^[34] Consequently, the appearance of isosbestic points demonstrated a good electrochemical interconversion between the neutral and reduced states. Notably, to further explore the doping mechanism and plasticity modulation relationship, the electrical stimuli time-dependent absorption has been performed (Figure S15), which presents a similar variation tendency with the bias-dependent absorption. Besides, both gNR-EG and gNR-Bu with variable type of side chain at the rhodamine motif exhibit hydrophilicity feature with contact angle for 36.4° and 45.1° respectively (Figure S16). The relatively high hydrophilic properties would facilitate both sn-OMIECs to bind the hydrated ions from the electrolyte and show hysteresis in the doping and dedoping process with no-volatility behaviors.

Next, we turned more attention to their microstructural properties. The microstructures of two thin-films were performed by grazing-incidence wide-angle X-ray scattering to investigate the impact of molecular packing and orientation modes on device performances discussed above. Extended data about crystallographic parameters see in Tables S2 and S3. As shown in Figure 4 and S17, both two materials display high degree of crystallinity, typical of small molecular OMIECs as previous reported,^[17b] with obvious three distinct (h00) peaks in the out-of-plane direction (OOP), indicating an ordered lamellar packing in both pristine and doped state of thin-films. They also showed more evident (010) diffraction peaks at in-plane direction than out-of-plane direction, suggesting a predominant edge-on orientation. In the pristine state, shorter π – π stacking distance of 3.42 Å was estimated for gNR-Bu, compared to that of gNR-EG for 3.48 Å. In addition, gNR-Bu shows larger Coherence lengths (CLs) values in both out-of-plane (167.2 Å) and in-plane (62.2 Å) orientation, a significant Figure of merit closely relative to crystallinity of semiconductors, than those of gNR-EG. The shorter distance of

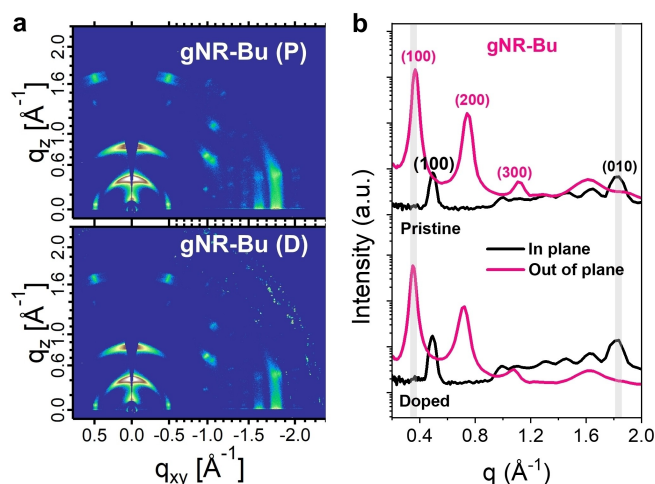


Figure 4. a) 2D-GIWAXS patterns of gNR-Bu thin films in pristine state (P) and doped state (D). b) Line-cut profiles of gNR-Bu films obtained by integration along the in-plane (q_{xy}) and out-of-plane (q_z) direction.

π – π stacking and larger CLs for gNR-Bu indicate a higher degree of crystallinity and ordered molecular packing, which might favor the hysteresis of ion motion throughout the crystallites and prevents H_2O and O_2 from permeating.^[35] These results might explain the good non-volatility and ambient stability observed in the gNR-Bu synaptic devices.

To simulate doped state with relevant conditions, we applied a bias gate voltage of -0.6 V for electrochemically reduction. It was clear from the Tables S2 and S3, both materials almost maintain original structural characterizations in π -stacking, π -stacking distances from 3.48 to 3.49 Å for gNR-EG, and from 3.42 to 3.43 Å for gNR-Bu, respectively. Markedly, in lamellar packing direction, gNR-Bu undergoes larger changes in lamellar distance at the (100) diffraction peak from 17.11 to 17.99 Å than those of gNR-EG from 16.70 to 16.79 Å. Besides, gNR-Bu keeps a larger CLs value for 163.2 Å relative to gNR-EG for 134.1 Å. In general, in comparison with gNR-EG, gNR-Bu undergoes more effective ions doping along with the maintenance of high crystallinity, suggesting that stronger lamellar packing interactions act in butyl chain of gNR-Bu, which enables gNR-Bu to modulate synaptic behavior robustly and efficiently by the bulky ions doping and transport.

Artificial synaptic devices can be operated in aqueous environments is still challenge.^[12] However, neurotransmitters directly affect the regulation of relevant brain function and their monitoring in biological environments is crucial to diagnose some brain diseases.^[36] To veritably simulate biological synapses communication in aqueous environments, such as Na^+ or dopamine (DA) neurotransmitters, an aqueous electrolyte was employed to mediate synaptic transmission by single-pulse-induced stimulus to respond different biological analytes. Based on previous device architecture,^[37] aqueous electrolyte is confined by a PDMS well and Pt wire as the gate electrode is inserted into electrolyte, the schematic as shown in Figure 5a. In aqueous electrolyte gated pattern with 0.1 M NaCl, both gNR-Bu

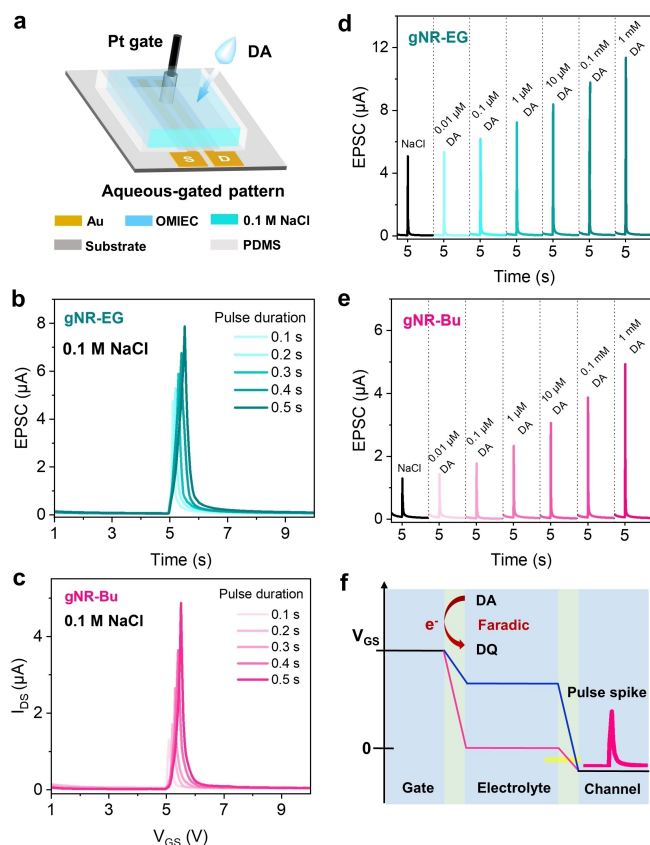


Figure 5. Synaptic behavior gated by aqueous electrolyte. a) Schematic of aqueous electrolyte gated device. STDP of b) gNR-EG and c) gNR-Bu devices gated by 0.1 M NaCl electrolyte with different t_{pre} ranging from 0.1 to 0.5 s under $V_{pre} = 1.0$ V. Single-pulse-induced response of d) gNR-EG and e) gNR-Bu devices to DA stimulation with different level ranging from 0.01 μ M to 1 Mm under $V_{pre} = 1.0$ V, $t_{pre} = 0.1$ s. f) Schematic of DA electrochemically oxidation to induce pulse spike.

and gNR-EG also display STDP modulated by a single pulse with t_{pre} ranging from 0.1 to 0.5 s (Figure 5b, c). The pulse spike (EPSC) increases accordingly along with increment of pulse duration, the feature in accordance with those in ion-gel gated pattern, which demonstrates the potential of two materials for modulating synaptic plasticity in aqueous condition. Besides, the pulse spike quickly returns to its initial value upon removing gate voltage (rang of ms to s), typical of volatility characteristics, which may attribute to the rapid movement of ions in aqueous environments and thereby result in hardly observed hysteresis of the transfer curve in the NaCl aqueous electrolyte (Figure S18), in accordance with the results of UV-vis-NIR spectroelectrochemistry. Noted that gNR-EG exhibits faster respond capability of combining hydrated ions (Na^+) due to its higher hydrophilicity, and thus induces higher level of pulse spike compared to gNR-Bu.

Beyond hydrated sodium, we further demonstrated the potential for detecting synapses communication signals of DA neurotransmitter in aqueous condition (Figure 5d, e). A single pulse ($V_{pre} = 1.0$ V, $t_{pre} = 0.1$ s) is applied to the gate dropped with different concentrations of DA analyte

ranging from 0.01 μ M to 1 mM. For the DA concentration < 0.1 μ M, the pulse spike keeps largely at the same level, which resembles the biological systems that the low stimulation intensity is insufficient to induce action potentials. As the DA concentration gradually increases from 1 μ M to 1 mM, the pulse spike shows a markedly increasing trend, indicating that high stimulation strength enables to reach the threshold of induced action potentials.^[15] Notably, gNR-EG displays more sensitive respond to low concentration of DA along with higher induced pulse spike, owing to its higher hydrophilicity facilitating to combine hydrated ions, with respect to gNR-Bu. Figure 5f illustrates the schematic of sensing various concentration of DA with pulse spike. The oxidized DA, i.e., dopaminquinone (DQ), leads to generate induced faradic currents, and thus benefits for lowering the potential drop at the interface between the gate and electrolyte.^[31] When DA concentration at a high level, a larger potential drop can bring about more effective gating to thereby generate a higher induced pulse spike. In general, our gNR-EG and gNR-Bu, as mediated OMIECs, enable to respond synaptic communication signals in biological aqueous environments like DA even at sub- μ M level, demonstrating their great potential in precise diagnosis of some diseases associated with neurotransmitter disorders.

Conclusion

We have experimentally demonstrated the first small-molecular n-type OMIECs based organic electrochemical neuronal synapse (sn-OENS). Such a sn-OENS exhibits superior artificial synapse characteristics in a single device with an unprecedented combination of facile fabrication, excellent ambient stability, robust and flexible tunability, learning and memory, signal separation, dynamic filtering, and image recognition, as well as to be high sensitivity DA neurotransmitter neuromorphic sensor in aqueous electrolyte. Markedly, OENS with gNR-Bu shows highly recognition accuracy of 94 % for a model ANN simulation, highly steady conductance states maintained over 600 s in ambient conditions, as well as excellent ambient stability with EPSC retained for 54 % after 100 days without any encapsulating or further treating. Very interesting self-repairing behaviors have been observed, the retention of EPSC can further improving to 90.9 % via briefly adjusting gate voltage as compensation. The superior synapse functions of the gNR-Bu were shown to its enhanced degree of crystallinity and ordered molecular packing. More impressively, in aqueous electrolyte gated pattern, gNR-EG and gNR-Bu based devices enable to sense synaptic communication signals like DA even at sub- μ M level. This small-molecular n-type OMIECs strategy may pave a way to building next bioelectronics integrated with sensing, memory and computing.

Acknowledgements

The work was supported by the National Key R&D Program (Grant No. 2022YFA1206600), National Natural Science Foundation of China (Grant No. 22275212), Guangdong Basic and Applied Basic Research Foundation (Grant No. 2022A1515110729), Fundamental Research Funds for the Central Universities, Sun Yat-sen University (Grant No. 23yxqntd002).

Conflict of Interest

The authors declare no conflict of interest.

Data Availability Statement

The data that support the findings of this study are available from the corresponding author upon reasonable request.

Keywords: Bioelectronics • Ionic–Electronic Conductors • N-Type Small-Molecule • Organic Electrochemical Neuronal Synapse

- [1] S. Wang, X. Chen, C. Zhao, Y. Kong, B. Lin, Y. Wu, Z. Bi, Z. Xuan, T. Li, Y. Li, W. Zhang, E. Ma, Z. Wang, W. Ma, *Nat. Electron.* **2023**, 6, 281–291.
- [2] R. Bhunia, E. K. Boahen, D. J. Kim, H. Oh, Z. Kong, D. H. Kim, *J. Mater. Chem. C* **2023**, 11, 7485–7509.
- [3] J. Chen, W. Huang, D. Zheng, Z. Xie, X. Zhuang, D. Zhao, Y. Chen, N. Su, H. Chen, R. M. Pankow, Z. Gao, J. Yu, X. Guo, Y. Cheng, J. Strzalka, X. Yu, T. J. Marks, A. Facchetti, *Nat. Mater.* **2022**, 21, 564–571.
- [4] R. Chen, A. Canales, P. Anikeeva, *Nat. Rev. Mater.* **2017**, 2, 16093.
- [5] H. H. Choudhry, D. H. Lee, A. Bag, N. E. Lee, *Nat. Commun.* **2023**, 14, 821.
- [6] P. C. Harikesh, C. Y. Yang, H. Y. Wu, S. Zhang, M. J. Donahue, A. S. Caravaca, J. D. Huang, P. S. Olofsson, M. Berggren, D. Tu, S. Fabiano, *Nat. Mater.* **2023**, 22, 242–248.
- [7] J. Rivnay, S. Inal, A. Salleo, R. M. Owens, M. Berggren, G. G. Malliaras, *Nat. Rev. Mater.* **2018**, 3, 17086.
- [8] B. D. Paulsen, K. Tybrandt, E. Stavrinidou, J. Rivnay, *Nat. Mater.* **2020**, 19, 13–26.
- [9] B. Zhou, W. Liu, Y. Xu, C. Jin, J. Yang, J. Sun, *J. Phys. D* **2022**, 55, 304006.
- [10] a) Y. van de Burgt, E. Lubberman, E. J. Fuller, S. T. Keene, G. C. Faria, S. Agarwal, M. J. Marinella, A. Alec Talin, A. Salleo, *Nat. Mater.* **2017**, 16, 414–418; b) L.-a. Kong, J. Sun, C. Qian, Y. Fu, J. Wang, J. Yang, Y. Gao, *Org. Electron.* **2017**, 47, 126–132; c) D.-G. Seo, Y. Lee, G.-T. Go, M. Pei, S. Jung, Y. H. Jeong, W. Lee, H.-L. Park, S.-W. Kim, H. Yang, C. Yang, T.-W. Lee, *Nano Energy* **2019**, 65, 104035.
- [11] P. Robin, T. Emmerich, A. Ismail, A. Niguès, Y. You, G.-H. Nam, A. Keerthi, A. Siria, A. K. Geim, B. Radha, L. Bocquet, *Science* **2023**, 379, 161–167.
- [12] T. Xiong, C. Li, X. He, B. Xie, J. Zong, Y. Jiang, W. Ma, F. Wu, J. Fei, P. Yu, L. Mao, *Science* **2023**, 379, 156–161.
- [13] a) H. Sun, J. Gerasimov, M. Berggren, S. Fabiano, *J. Mater. Chem. C* **2018**, 6, 11778–11784; b) S. Griggs, A. Marks, H. Bristow, I. McCulloch, *J. Mater. Chem. C* **2021**, 9, 8099–8128.
- [14] W. Huang, J. Chen, Y. Yao, D. Zheng, X. Ji, L. W. Feng, D. Moore, N. R. Glavin, M. Xie, Y. Chen, R. M. Pankow, A. Surendran, Z. Wang, Y. Xia, L. Bai, J. Rivnay, J. Ping, X. Guo, Y. Cheng, T. J. Marks, A. Facchetti, *Nature* **2023**, 613, 496–502.
- [15] X. Xu, H. Zhang, L. Shao, R. Ma, M. Guo, Y. Liu, Y. Zhao, *Angew. Chem. Int. Ed.* **2023**, 62, e202302723.
- [16] a) G. Dolen, A. Darvishzadeh, K. W. Huang, R. C. Malenka, *Nature* **2013**, 501, 179–184; b) F. Sun, J. Zeng, M. Jing, J. Zhou, J. Feng, S. F. Owen, Y. Luo, F. Li, H. Wang, T. Yamaguchi, Z. Yong, Y. Gao, W. Peng, L. Wang, S. Zhang, J. Du, D. Lin, M. Xu, A. C. Kreitzer, G. Cui, Y. Li, *Cell* **2018**, 174, 481–496.
- [17] a) J. Duan, G. Zhu, J. Chen, C. Zhang, X. Zhu, H. Liao, Z. Li, H. Hu, I. McCulloch, C. B. Nielsen, W. Yue, *Adv. Mater.* **2023**, 35, e2300252; b) J. Duan, G. Zhu, L. Wang, J. Chen, S. Cong, X. Zhu, Y. Zhou, Z. Li, I. McCulloch, W. Yue, *Adv. Funct. Mater.* **2022**, 32, 2203937.
- [18] C. Wang, H. Dong, W. Hu, Y. Liu, D. Zhu, *Chem. Rev.* **2011**, 112, 2208–2267.
- [19] a) X. Zhu, J. Duan, J. Chen, R. Liu, Z. Qin, H. Chen, W. Yue, *Angew. Chem. Int. Ed.* **2023**, 62, e202311879; b) X. Zhang, C. Li, L. Qin, H. Chen, J. Yu, Y. Wei, X. Liu, J. Zhang, Z. Wei, F. Gao, Q. Peng, H. Huang, *Angew. Chem. Int. Ed.* **2021**, 60, 17720–17725; c) Z. G. Zhang, Y. Li, *Angew. Chem. Int. Ed.* **2021**, 60, 4422–4433.
- [20] a) H. Chen, Y. Sun, M. Liu, F. Li, Q. Peng, H. Huang, *Angew. Chem. Int. Ed.* **2023**, 62, e202302629; b) H. Huang, L. Yang, A. Facchetti, T. J. Marks, *Chem. Rev.* **2017**, 117, 10291–10318; c) C. Li, X. Gu, Z. Chen, X. Han, N. Yu, Y. Wei, J. Gao, H. Chen, M. Zhang, A. Wang, J. Zhang, Z. Wei, Q. Peng, Z. Tang, X. Hao, X. Zhang, H. Huang, *J. Am. Chem. Soc.* **2022**, 144, 14731–14739; d) M. Liu, X. Han, H. Chen, Q. Peng, H. Huang, *Nat. Commun.* **2023**, 14, 2500.
- [21] S. J. Kim, J. S. Jeong, H. W. Jang, H. Yi, H. Yang, H. Ju, J. A. Lim, *Adv. Mater.* **2021**, 33, e2100475.
- [22] W. Wang, Z. Li, M. Li, L. Fang, F. Chen, S. Han, L. Lan, J. Chen, Q. Chen, H. Wang, C. Liu, Y. Yang, W. Yue, Z. Xie, *Nano-Micro Lett.* **2022**, 14, 184.
- [23] Z. Qin, D. Dong, M. Yao, Q. Yu, X. Sun, Q. Guo, H. Zhang, F. Yao, J. Li, *ACS Appl. Mater. Interfaces* **2019**, 11, 21184–21193.
- [24] Y. Zhang, G. Ye, T. P. A. van der Pol, J. Dong, E. R. W. van Doremaele, I. Krauhausen, Y. Liu, P. Gkoupidenis, G. Portale, J. Song, R. C. Chiechi, Y. van de Burgt, *Adv. Funct. Mater.* **2022**, 32, e2201593.
- [25] R. S. Zucker, W. G. Regehr, *Annu. Rev. Physiol.* **2002**, 64, 355–405.
- [26] Z. Xie, C. Zhuge, Y. Zhao, W. Xiao, Y. Fu, D. Yang, S. Zhang, Y. Li, Q. Wang, Y. Wang, W. Yue, I. McCulloch, D. He, *Adv. Funct. Mater.* **2022**, 32, e2107314.
- [27] H. Shim, F. Ershad, S. Patel, Y. Zhang, B. Wang, Z. Chen, T. J. Marks, A. Facchetti, C. Yu, *Nat. Electron.* **2022**, 5, 660–671.
- [28] S. Wang, C. Chen, Z. Yu, Y. He, X. Chen, Q. Wan, Y. Shi, D. W. Zhang, H. Zhou, X. Wang, P. Zhou, *Adv. Mater.* **2019**, 31, e1806227.
- [29] Y. Zhao, C. Su, G. Shen, Z. Xie, W. Xiao, Y. Fu, S. Inal, Q. Wang, Y. Wang, W. Yue, I. McCulloch, D. He, *Adv. Funct. Mater.* **2022**, 32, e2205744.
- [30] X. Liu, C. Sun, Z. Guo, X. Xia, Q. Jiang, X. Ye, J. Shang, Y. Zhang, X. Zhu, R. W. Li, *Adv. Sci.* **2023**, 10, e2300471.
- [31] Y. Zhang, E. R. W. van Doremaele, G. Ye, T. Stevens, J. Song, R. C. Chiechi, Y. van de Burgt, *Adv. Mater.* **2022**, 34, e2200393.
- [32] a) Y. Zhao, S. Haseena, M. K. Ravva, S. Zhang, X. Li, J. Jiang, Y. Fu, S. Inal, Q. Wang, Y. Wang, W. Yue, I. McCulloch, D. He, *Nano Energy* **2022**, 104, e107985; b) E. J. Fuller, F. E. Gabaly, F. Leonard, S. Agarwal, S. J. Plimpton, R. B. Jacobs-

- Gedrim, C. D. James, M. J. Marinella, A. A. Talin, *Adv. Mater.* **2017**, 29, e1604310.
- [33] X. Zhan, A. Facchetti, S. Barlow, T. J. Marks, M. A. Ratner, M. R. Wasielewski, S. R. Marder, *Adv. Mater.* **2011**, 23, 268–284.
- [34] I. Zozoulenko, A. Singh, S. K. Singh, V. Gueskine, X. Crispin, M. Berggren, *ACS Appl. Polym. Mater.* **2019**, 1, 83–94.
- [35] Y. Wang, E. Zeglio, L. Wang, S. Cong, G. Zhu, H. Liao, J. Duan, Y. Zhou, Z. Li, D. Mawad, A. Herland, W. Yue, I. McCulloch, *Adv. Funct. Mater.* **2022**, 32, e2111439.
- [36] W. Li, J. Jin, T. Xiong, P. Yu, L. Mao, *Angew. Chem. Int. Ed.* **2022**, 61, e202204134.
- [37] J. Chen, S. Cong, L. Wang, Y. Wang, L. Lan, C. Chen, Y. Zhou, Z. Li, I. McCulloch, W. Yue, *Mater. Horiz.* **2023**, 10, 607–618.
- Manuscript received: October 16, 2023
Accepted manuscript online: December 11, 2023
Version of record online: December 22, 2023
-